J Mater Sci: Mater Electron (2022) 33:19734–19750

Growth, first-principles simulations and near-infrared optical properties of rare earth (Nd^{3+}, Er^{3+})-doped CeF_3 crystals for laser applications

Weiling Yang[1], Xiliang Jiang[1], Zhuang Leng[1], Huisheng Liu[1], Ce Li[4], Zhiming Shi[3],
KeKe Huang[5], Fanming Zeng[1,2,*], Chun Li[1,2,*], Hai Lin[1,2], and Zhongmin Su[1,2,*]

[1] *School of Materials Science and Engineering, Changchun University of Science and Technology, Changchun 130022, China*
[2] *Collaborative Innovation Center of Optical Materials and Chemistry, Changchun University of Science and Technology, Changchun 130022, China*
[3] *Changchun Institute of Optics, Fine Mechanics and Physics, Chinese Academy of Sciences, Jilin University, Changchun, China*
[4] *Southwest Institute of Technical Physics, Chengdu 610041, China*
[5] *State Key Laboratory of Inorganic Synthesis and Preparative Chemistry, College of Chemistry, Jilin University, Changchun 130012, People's Republic of China*

Received: 19 May 2022
Accepted: 8 July 2022

ABSTRACT

Nd^{3+}:CeF_3 and Er^{3+}:CeF_3 crystals with different doping concentrations were successfully grown by the Bridgman method. The physicochemical parameters, such as crystal structure and phonon vibration energy were obtained by XRD and Raman tests. The results show that rare earth (Nd^{3+} or Er^{3+}) does not change the hexagonal phase structure of the crystal, and the doping of rare earth ions does not change the maximum phonon frequency. The measured results are 388 and 392 cm^{-1}, respectively, which are similar to CeF_3 single crystal and half of common oxide crystal. According to the first principle, the difference charge density of the two crystals can be intuitively obtained. The calculated band gap values of the two crystals are 2.91 and 4.37 eV, respectively, which are similar to the results of absorption spectrum measurement. The NIR luminescence performance of Nd^{3+}:CeF_3 crystal was tested by 808 nm pump. When the doping concentration reached 2 at%, the emission intensity was the strongest at 1064 nm ($^4F_{3/2}\rightarrow{}^4I_{11/2}$). The luminescence properties of Er^{3+}:CeF_3 crystal at 1550 nm ($^4I_{13/2}\rightarrow{}^4I_{15/2}$) were tested by 980 nm pump. The emission intensity keeps the highest when the doping concentration reaches 3 at%. The concentration quenching and the dipole-dipole interaction in crystals are studied using energy transfer theory, and the J-O strength parameters of crystals are calculated. The results show that Nd^{3+}:CeF_3 and Er^{3+}:CeF_3 crystals have excellent properties and excellent near-infrared luminescence performance, which has great potential in laser applications.

Address correspondence to E-mail: zengfm@126.com; lichun1210@163.com; zmsu@nenu.edu.cn

Springer

https://doi.org/10.1007/s10854-022-08747-z

1 Introduction

In recent years, near-infrared lasers have been widely used in machining, environmental monitoring, radar communication, and medical instruments [1–3]. As the core of the laser, performing the working medium determines the output capability of the laser. Compared with glass or ceramics, laser crystal materials have stronger stability and higher laser output efficiency [4]. However, the research of traditional oxide crystals, such as garnet, tungstate crystal and vanadate, has reached the bottleneck, and it is difficult to improve the performance greatly [5]. There are also some shortcomings, such as insufficient thermal stability and easy segregation of components. Therefore, it is important and meaningful to develop new crystal materials [6–10]. Among many crystal materials, fluoride matrix crystal has become the focus because of its low phonon energy, easy uniform doping and stable physical and chemical properties [11–14]. CeF_3 crystal used to be a scintillator or magneto-optical crystal has attracted much attention. Recently, CeF_3 crystals have been found to be a good laser crystal matrix. For example, Dy^{3+}:CeF_3 crystals and Ho^{3+}:CeF_3 crystals have been proved to have excellent luminous properties in visible and mid-infrared bands, and can be used as a new generation of laser working media [15–20]. But there is not much progress in the near-infrared

At present, the specific excitation wavelength of Nd^{3+} ion 808 nm is one of the most widely used pump sources in the market, and its emission wavelength of 1064 nm is widely used in medical beauty and other fields [21, 22]. In addition, the excellent performance of Er^{3+} in many crystal materials, which is also used as an active ion, has aroused great interest of researchers. Er^{3+} ion has rich energy level structure. The 1.5–1.6 μm transition based on $^4I_{13/2} \rightarrow {}^4I_{15/2}$ is widely used in optical communication, medical treatment and laser ranging [23]. Therefore, among all the rare earth elements, only Nd^{3+} and Er^{3+} have unique emission wavelengths in the near-infrared band [24]. These two elements are similar in structure and size to Ce^{3+} ions in CeF_3 crystal. In the process of doping, it can be substituted to avoid defects and dislocation, to ensure good luminescence performance of the crystal [25].

However, there is little research on Nd^{3+} or Er^{3+} ion-doped CeF_3 crystal, especially the related electronic structure, physical and chemical properties and near-infrared emission properties after doping, which greatly limits the application of CeF_3 crystal in the optical field. Therefore, it is necessary to carry out systematic and complete research on Nd^{3+} or Er^{3+} ion-doped CeF_3 crystal. The luminescence properties of Nd^{3+}:CeF_3 and Er^{3+}:CeF_3 crystals in the near-infrared band (1064 and 1550 nm) were further studied to obtain the performance of the crystals as the working medium of the laser, so as to develop the advantages and values of the crystals in the field of near-infrared laser output [26–28].

In this study, Nd^{3+} or Er^{3+} ion-doped CeF_3 crystals were successfully grown by crucible descent method. The phase properties were analyzed and characterized by XRD, Raman and density. The electronic structures of these two rare earth-doped crystals are simulated by first-principles and their influences on the near-infrared optical properties of the crystals are analyzed. The related parameters and properties of the crystals are further analyzed and explored by combining J-O calculation and energy transfer theory, so as to further expand the application value of the crystals in the near-infrared field.

2 Crystal growth

The Nd^{3+}:CeF_3 and Er^{3+}:CeF_3 crystal was grown by the Bridgeman-Stockbarge method. Firstly, the polycrystalline materials were dried and fluorinated. Next, the polycrystalline material was mixed with deoxidizer (PbF_2 2 wt%) and loaded into a platinum crucible. Polycrystalline material filling volume accounts for about 2/3 of the volume of the crucible, to prevent the mixture from volatilizing leading to cracking of the crucible. The crucible is evacuated and welded sealed. Then the processed crucible is put into the lifting device, lifted into the furnace and heated to 1630 °C, and the crystal begins to grow. During the growth process, the descending rate of the crucible was adjusted to 0.5–1.2 mm/h, and the cooling program was about 35 °C/h. After cooling to room temperature, the crystal was taken out and processed. Figure 1 shows photographs of the Nd^{3+} or Er^{3+}:CeF_3 crystals.

3 Analysis and discussion

3.1 Structural analysis and characterization

As shown in Fig. 2a, b, a series of XRD data patterns of Re^{3+}(Nd, Er):CeF_3 crystals are shown. The crystal phase structure of the crystals was examined by X-ray diffraction (XRD), and several well-defined diffraction peaks appeared in the pattern confirmed the existence of hexagonal CeF_3 crystals. All peak positions are consistent with the standard card of hexagonal CeF_3 crystal (JCPDS No.08-0045), all the grown crystals have good resolution and standard diffraction patterns. Hence, no obvious impurity peaks were detected, confirmed that the crystal quality was good. Moreover, that it was not oxidized and no impurity phase was generated in the crystal. Figure 3 can visualize this doping process. Figure 4 shows the scanning electron microscope image of the crystal sample (SEM). Figure 4a, c are SEM images of Nd^{3+}:CeF_3 crystal at different magnifications. It can be seen that there is no fracture, showing a complete overall structure, indicating that the crystals grown are of good quality. The irregular structure of surface undulation results from crystal cutting and polishing. Figure 4 d–f belong to SEM images of Er^{3+}:CeF_3 crystal at different magnifications. As shown in Fig. 4, the crystal surface is also very dense, without obvious fractures and defects, with a complete structure and good quality [29].

3.2 Raman spectroscopy

Among the overall optical properties of crystals, lattice vibration energy (phonon frequency) is an important factor affecting the optical properties of crystals. High phonon energy will cause too much transition energy to be converted into non-radiative transition energy by phonon absorption, resulting in a significant decrease in the efficiency of radiative transition [30]. Figure 5a, b are the Raman spectra of 3 at% Nd^{3+}:CeF_3 and 3 at% Er^{3+}:CeF_3 crystal, respectively. Using 325 nm as the laser source band, and the test wavenumber range is 0–1000 cm^{-1}. It can be observed that among the several characteristic peaks exhibited by these two crystals, the characteristic peaks with the highest intensity (388 and 392 cm^{-1}) are the maximum phonon frequency of the crystals. This is close to the maximum phonon frequency of pure CeF_3 single crystal reported in the literature [15]. This shows that the doping of different rare earth elements does not change the crystal structure and does not lead to an increase in phonon frequency. The maximum phonon frequency of crystals is obviously lower than that of common crystals such as tungstate, vanadate and garnet [31]. This effectively reduces the radiation-free transition probability and increases the fluorescence lifetime of the upper level. In laser applications, it is easier to realize particle number inversion and improve the overall light output efficiency.

3.3 Density analysis

Among the numerous properties of crystals, density is an important physicochemical parameter to characterize the properties of crystals. The density of Re^{3+}(Nd, Er):CeF_3 crystals was tested by the Archimedes drainage method. The times of tests for each sample is not less than 3 times, and the average value is taken to reduce the error. As shown in Fig. 6a and b, it can be seen that as the doping concentration of Nd^{3+} or Er^{3+} ions increase, the densities of the crystals show an upward trend, which are larger than that of the pure CeF_3 crystal (6.1225 g/cm^3) [15]. This phenomenon can be attributed to that the atomic

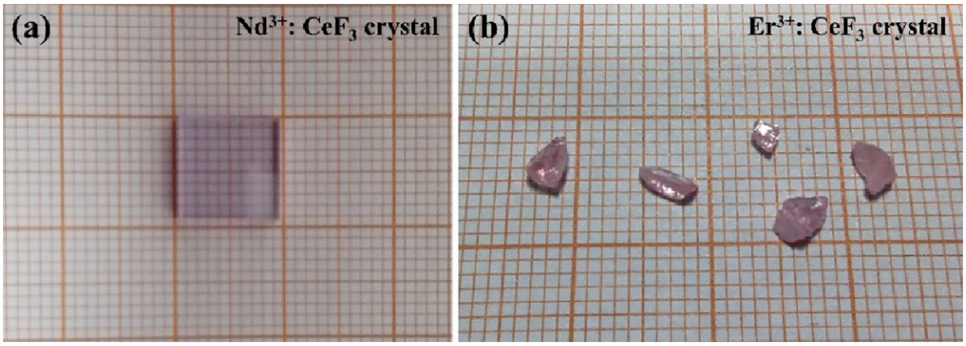

Fig. 1 Crystals grown by the crucible descending method **a** Nd^{3+}:CeF_3 crystal; **b** Er^{3+}:CeF_3 crystal

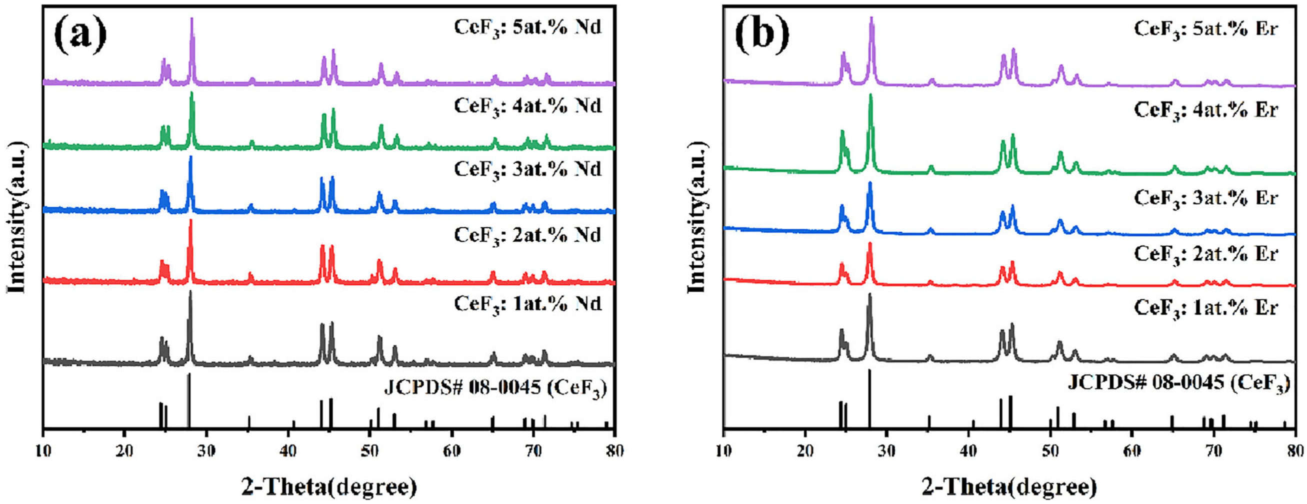

Fig. 2 **a** XRD patterns of CeF_3 crystals doped with different Nd^{3+} ion concentrations; **b** XRD patterns of CeF_3 crystals doped with different Er^{3+} ion concentrations

Fig. 3 Crystal structure and schematic diagram of rare earth-doped CeF_3

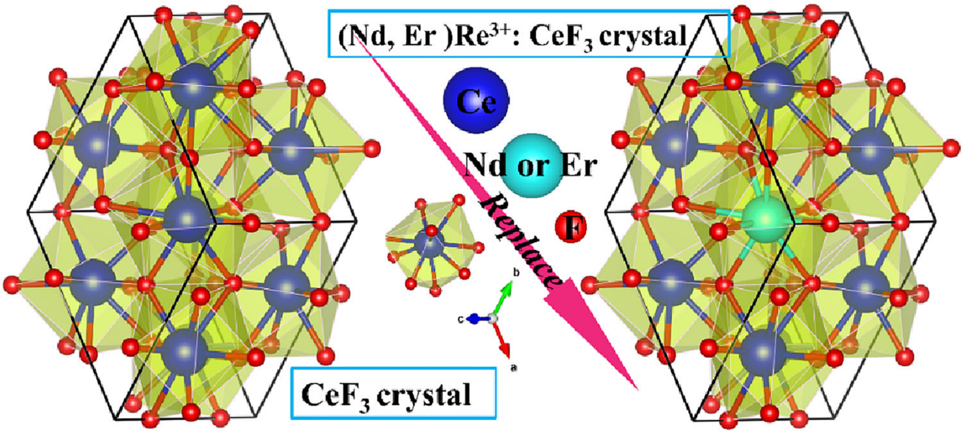

Fig. 4 SEM images of the two crystals, **a–c** are SEM images of Nd^{3+}:CeF_3 crystals at different magnifications; **d–f** SEM images belonging to Er^{3+}:CeF_3 crystals at different magnifications

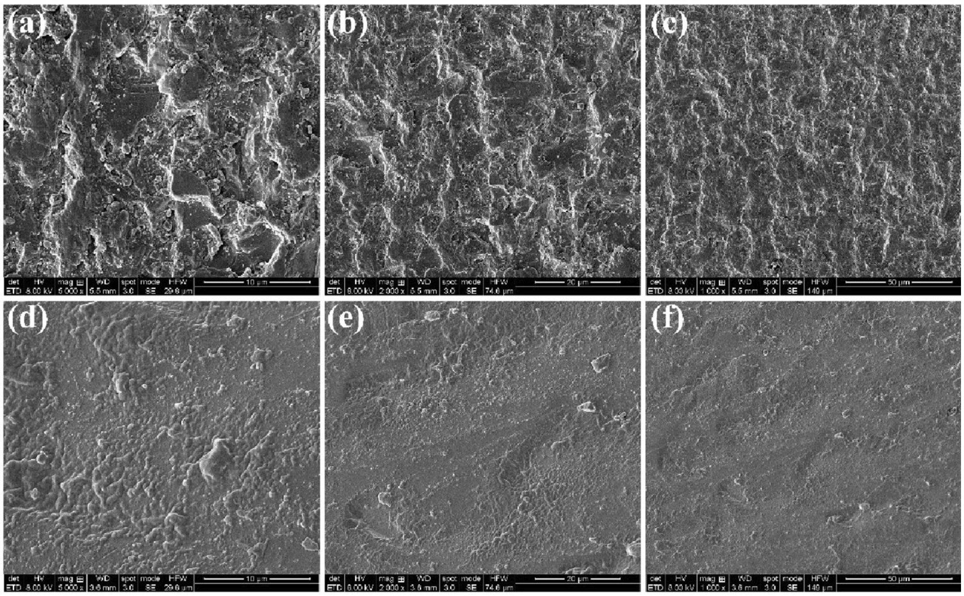

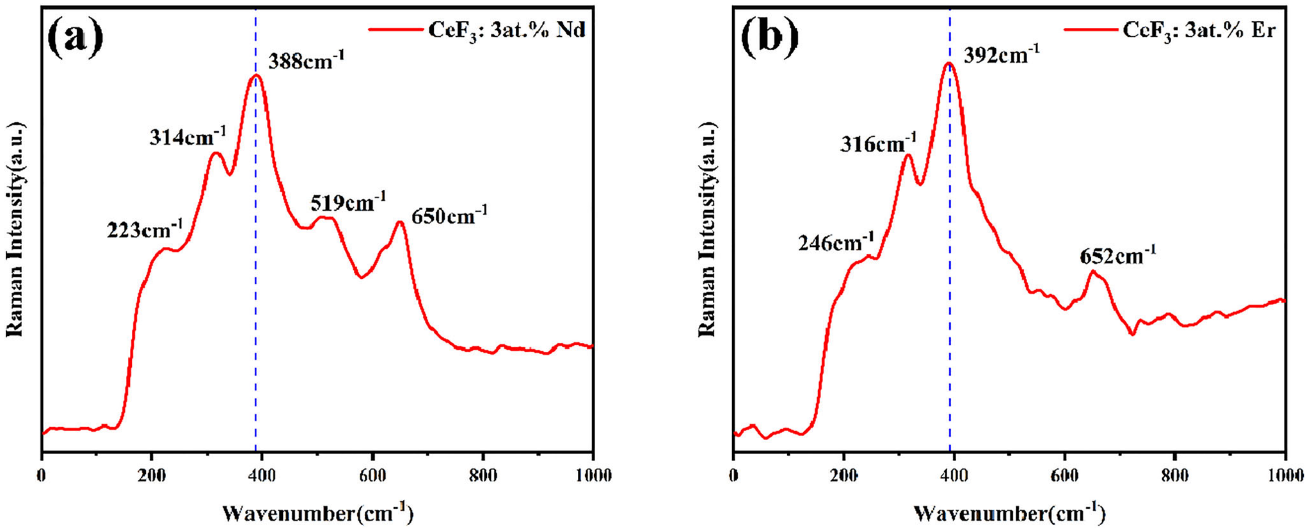

Fig. 5 **a** Raman spectrum of 3 at% Nd^{3+}:CeF_3 crystal, the excitation wavelength is 325 nm; **b** Raman spectrum of 3 at% Er^{3+}:CeF_3 crystal, 325 nm is selected as the excitation wavelength

mass of Nd^{3+} or Er^{3+} ions is larger than that of Ce^{3+} ions, and the lattice volume does not change much after para-substitution, but the overall mass increases slightly, so the density increases with the increase of doping concentration. Table 1 lists the density values under different doping concentrations in detail.

3.4 Absorption spectrum analysis

In order to study the optical energy levels of Nd^{3+}:CeF_3 and Er^{3+}:CeF_3 crystals in the near-infrared and visible range, the absorption spectra of Nd^{3+}:CeF_3 crystals at room temperature is recorded in Fig. 7a. In 300–1700 nm, six absorption peaks of Nd^{3+} ions were observed, and these absorption peaks at 517, 575, 677, 739, 803 and 864 nm correspond to the transition of the $^4I_{9/2}$ energy level to $^4G_{7/2}+^4G_{9/2}+^2K_{13/2}$, $^2G_{7/2}+^4G_{5/2}$, $^4F_{9/2}$, $^4F_{7/2}+^4S_{3/2}$, $^4F_{5/2}+^2H_{9/2}$ and $^4F_{3/2}$ energy levels [32]. These transition absorptions all come from the 4f-4f electronic transition process of Nd^{3+} ions. The absorption intensity at 575 nm ($^2G_{7/2}+^4G_{5/2}$) is the highest, followed by the absorption intensity at 803 nm ($^4F_{5/2}+^2H_{9/2}$), and the absorption intensity of the other four absorption peaks is

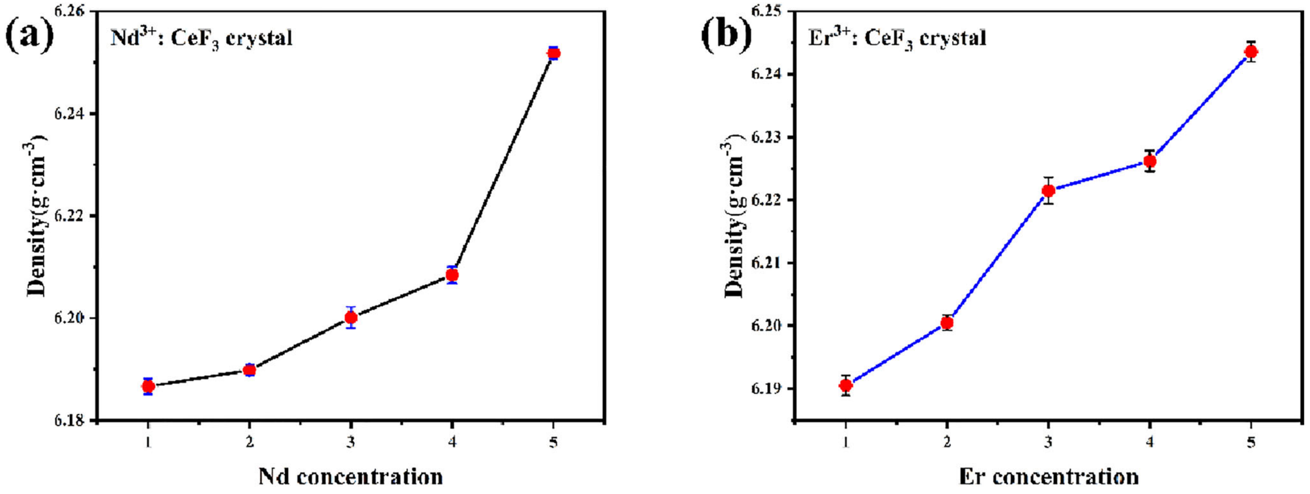

Fig. 6 Crystal density data obtained by measurement, **a** density variation curve of Nd^{3+}:CeF_3 crystals; **b** density variation curve of Er^{3+}:CeF_3 crystals

Table 1 Density values of crystals with different doping concentrations

Crystal	Density(g·cm^{-3})
1at. % Nd^{3+}:CeF_3	6.1866
2at. % Nd^{3+}:CeF_3	6.1897
3at. % Nd^{3+}:CeF_3	6.2013
4at. % Nd^{3+}:CeF_3	6.2085
5at. % Nd^{3+}:CeF_3	6.2517
1at. % Er^{3+}:CeF_3	6.1905
2at. % Er^{3+}:CeF_3	6.2005
3at. % Er^{3+}:CeF_3	6.2215
4at. % Er^{3+}:CeF_3	6.2262
5at. % Er^{3+}:CeF_3	6.2435

relatively weak, which is consistent with the results in other literatures on Nd^{3+} ion-doped crystals and glasses [33, 34]. This makes the crystal suitable for pumping by commercially available 808 nm, which increases the commercial potential of Nd^{3+}:CeF_3 crystals in near-infrared lasers. Figure 7b shows the absorption spectra of Er^{3+}:CeF_3 crystals in 250–1700 nm. Although some absorption peaks overlap slightly with adjacent energy levels and the background absorption is strong in the range of 250–400 nm, the diffraction peak positions are similar in these crystals, and the typical Er^{3+} ion absorption band is obvious [35–37]. When the Er ion is in the + 3 valence state, the erbium ion has 11 electrons in the 4f shell and the ground state is $^4I_{15/2}$. The absorption bands at $^4F_{9/2}$ and $^4I_{9/2}$ appear in the 618–680 and 780–840 nm [38, 39]. The $^4I_{11/2}$ band ranges from 940 to 1030 nm, with the strongest absorption at 980 nm. It well-matched with existing commercial 980 nm diode and fiber laser. In addition, the larger FWHM of absorption peak can reduce the temperature dependence of laser output and improve laser efficiency [40]. The absorption band at 1400–1600 nm results from the transition from the ground state $^4I_{15/2}$ to the high-energy state $^4I_{13/2}$.

3.5 First-principles simulation

First-principles simulation is increasingly used in crystal research. It can characterize and support the structure, charge distribution and physicochemical properties of crystal [41]. The doping structure was constructed, optimized and calculated by VASP. The PBE + U method was used in all the calculation processes, and the truncation energy was set at 500 eV. For the rare earth ion Ce^{3+} in matrix crystal, the *U* value of 4f orbital is set as 5 eV, and the 2p orbital of F is set as 4.5 eV. Doped elements Nd^{3+} and Er^{3+} are not added with *U* value. Figure 8a and b show the differential charge density obtained by calculation, and the bonding and polarization in the CeF_3 crystal after doping can be observed. With the doping of Nd^{3+} and Er^{3+} ions, the electrons near Ce^{3+} ions are close to the doped ions, and the charge

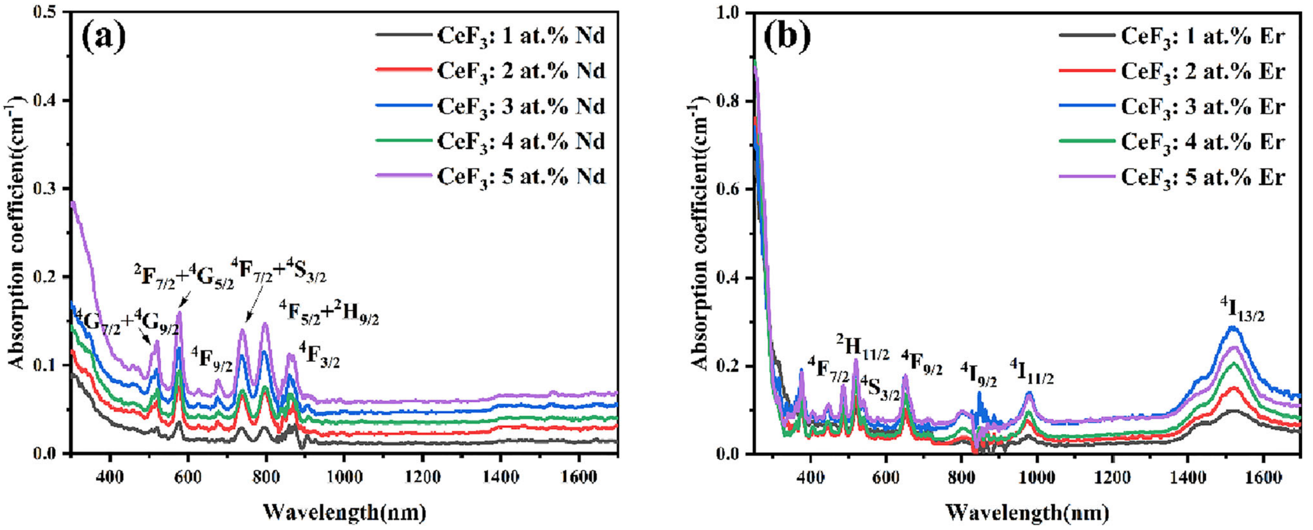

Fig. 7 **a** Absorption spectra of Nd^{3+}:CeF_3 crystals with different Nd^{3+} ions doping concentrations; **b** Absorption spectra of Er^{3+}:CeF_3 crystals with different Er^{3+} ions doping concentrations

density near the internal doped ions increases [42]. By comparing the differences in Fig. 8a and b, it can be found that the charge density near Er^{3+} ion is higher than that near Nd^{3+} ion, and the influence range is wider. This is mainly attributed to the stronger polarization intensity of Er^{3+} ion compared with Nd^{3+} ion, which will show more abundant energy levels and transition wavelengths in a macroscopic view in terms of optical properties [43].

In order to further explore the influence of doping rare earth ions on crystal electronic structure, the band structure of crystal was simulated. The band gap structures were calculated along the set Brillouin region path (G→X→H→C→H→Y →G), and the position of 0 point corresponds to the Position of Fermi level (E_F). Figure 9a shows the band structure of Nd^{3+}:CeF_3 crystal, and the calculated band gap width is about 2.91 eV. Figure 9b shows the band gap value calculated based on absorption spectrum (about 2.3–2.7 eV), and the average difference between theoretical and actual calculated values is about 0.4 eV. Figure 10a shows the band structure of Er^{3+}:CeF_3 crystal. The band gap obtained by simulation is about 4.37 eV. Compared with the band gap width calculated by test in Fig. 10b (about 3.29–3.83 eV), the average difference between theoretical and actual calculated values is only about 0.8 eV. By comparing the two simulated bandgap results, it can be found that although the types of rare earth elements doped are different, they do not change the characteristics that the lowest point of conduction band and the highest point of valence band are not completely corresponding in the horizontal normal direction, indicating that phonons are needed to balance the angular momentum in the transition process [44]. Therefore, doping does not change the indirect band gap structure of CeF_3 crystal, and phonons play an important role in the optical transition process, which is consistent with the Raman spectrum test results. However, compared with pure CeF_3 crystal, the change is reflected in the obvious fluctuation of conduction band, and the superposition of electronic states is more intensive, which also confirms that there will be efficient active states in the luminescence process after doping. In addition, there are some differences between simulation calculations and test calculations. This may be related to the test error and the setting of U value in the calculation process, on the other hand, it may also be caused by the absorption spectrum test error.

Next, as shown in Fig. 11, state densities of Nd^{3+}:CeF_3 and Er^{3+}:CeF_3 crystal were obtained to characterize the influence of doping ions on the luminescence process. In Fig. 11a, above Fermi level, the 4f and 5d electron layers of Ce^{3+} ions are relatively active, while the 4f state of Nd^{3+} ion is relatively active. These levels mainly determine the luminescence properties of the crystal. The 4f state of Nd^{3+} ion provides a relatively stable central level line of luminescence, which reduces the dispersion energy consumption in the process of energy level transition, which is conducive to the near-infrared luminescence of the crystal. Meanwhile, the 4f state of Ce^{3+} ion and the 4f state of Nd^{3+} ion overlap, so there

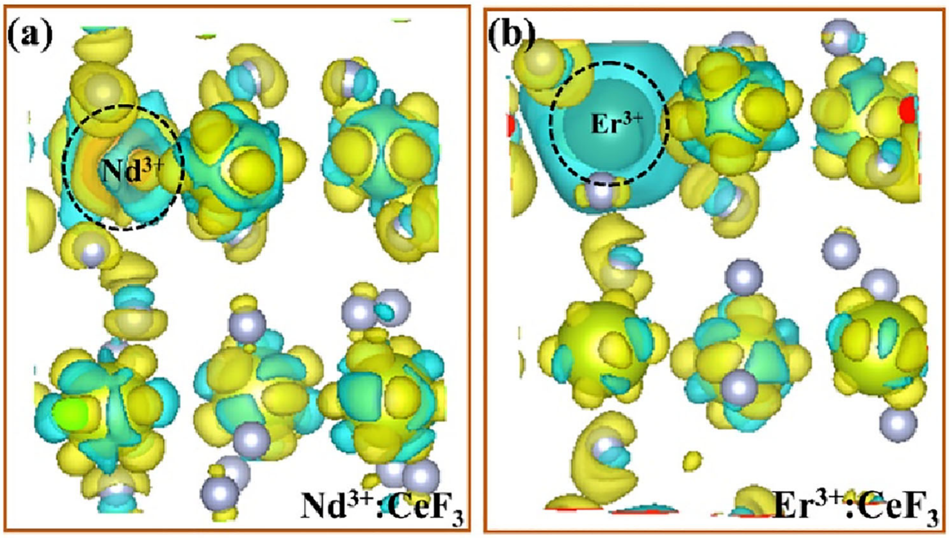

Fig. 8 The differential charge density, **a** differential charge density of Nd^{3+}:CeF_3 crystal; **b** differential charge density of Er^{3+}:CeF_3 crystal

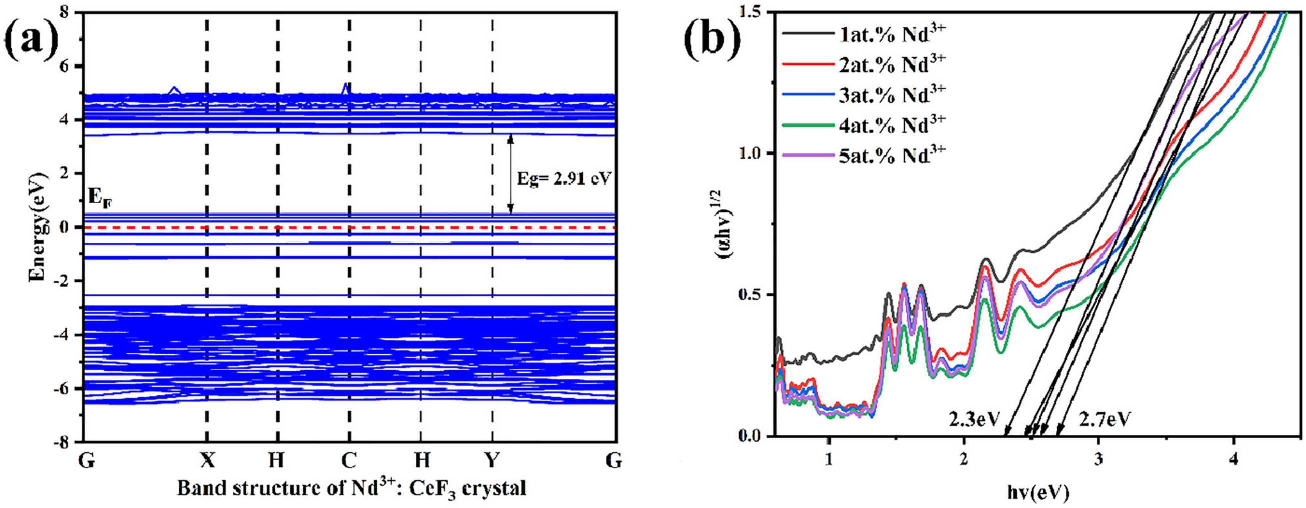

Fig. 9 **a** Band structure of Nd^{3+}:CeF_3 crystal calculated by first-principles calculation; **b** Band gap width value calculated from absorption spectrum data

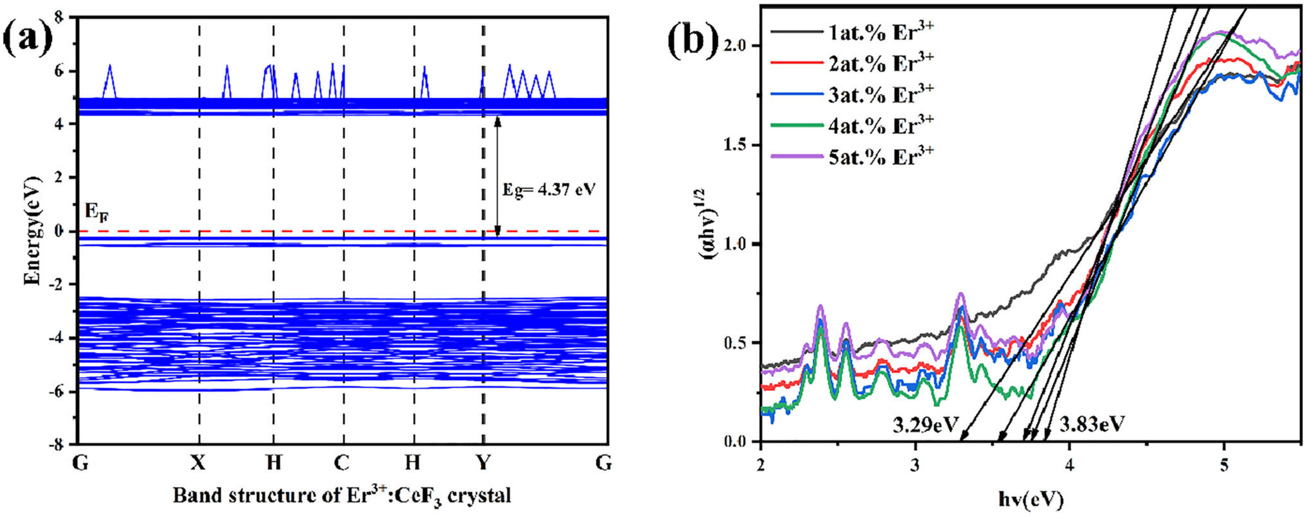

Fig. 10 **a** Band structure of Er^{3+}:CeF_3 crystal calculated by first-principles calculation; **b** Band gap width value calculated from absorption spectrum data

is also an energy transfer process during luminescence. At the same time, it can also be seen that the wave peaks of 4f and 5d electronic states of Nd^{3+} located on both sides of Fermi level (0 eV) correspond to the smaller energy level width, which directly reflects the weak covalence and stronger ionic property of bonding in the crystal [45]. In Fig. 11b, the 4f and 5d electron layers of Ce^{3+} ions are located on both sides of Fermi energy level with high contribution, indicating that in the process of NIR luminescence, the effect of Ce^{3+} ion cannot be ignored and will participate in the process of energy transfer. The 5d state of Er^{3+} ion is located above the conduction band, indicating that Er^{3+} has a high contribution to the NIR luminescence process. In addition, 4f state of Ce appears near Fermi level, and 5d state is located in conduction band, indicating that the transition process conforms to 4f-5d transition. For Er^{3+} ions, the distribution of 5d state is wide, and the distribution of the downward projection orbital is high, and the contribution is great [46]. However, 4f state is not shown in the figure, which is relatively delocalized. It may be distributed in a higher conduction band structure due to the setting of abscissa calculation.

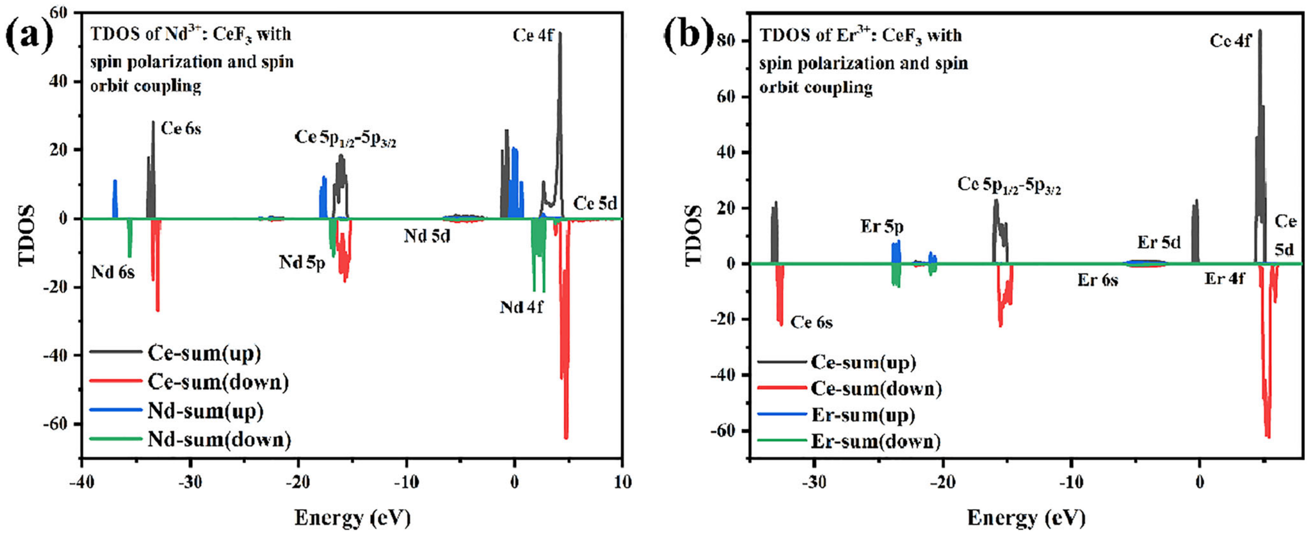

Fig. 11 **a** Calculated density of states of each cation in Nd^{3+}:CeF_3 crystal and distribution in different directions; **b** Calculated density of states of each cation in Er^{3+}:CeF_3 crystal and distribution in different directions

3.6 Near-infrared spectral characteristics

In order to further understand the NIR luminescence characteristics of Nd^{3+}:CeF_3 crystal, the NIR emission spectra of the crystal under 808 nm excitation were tested, as shown in Fig. 12a. There are two obvious emission bands in the range of 980–1500 nm. One is a strong emission band centered at 1064 nm, and the other is a relatively weak wide emission band centered at 1330 nm. The two excitation processes correspond to the energy level transition processes of $^4F_{3/4}$→$^4I_{11/2}$ (1064 nm) and $^4F_{3/4}$ →$^4I_{13/2}$ (1330 nm), respectively [47]. With the increase of Nd^{3+} ions doping concentration, the emission intensity of fluorescence spectrum increases gradually. When the doping concentration is 2 at%, the emission intensity is the strongest. With the further increase of the doping concentration, the emission spectrum gradually weakens, which is attributed to the concentration quenching phenomenon caused by the high doping concentration. Due to the high concentration of Ce^{3+} ions in the matrix, Ce^{3+} ions affect the luminescence process of Nd^{3+}:CeF_3 crystals. Therefore, in the analysis of spectral characteristics and energy level transition process [48], the role of Ce^{3+} ions in it cannot be ignored.

In general, when Ce^{3+} and Nd^{3+} ions appear in the crystal at the same time, Ce^{3+} ions will produce certain sensitization effect on Nd^{3+} ions in general. However, when excitation at 808 nm is used, with the increase of Nd^{3+} ion concentration and the relative decrease of Ce^{3+} ion concentration, the position of the obvious excitation peak at 1064 nm is almost the same, only the intensity changes. In general, Ce^{3+} ions in CeF_3 have excitation and emission processes in the 300–400 nm range, corresponding to $^2F_{5/2}$ and $^2F_{7/2}$ transitions to 5d levels. Therefore, in this range, there is excitation wavelength overlap between the two rare earth ions, indicating that the energy level position is similar. This usually results in a non-radiative relaxation process of energy transfer between the two rare earth ions. As can be seen from the energy level transition diagram in Fig. 12b, an energy transfer process involving radiation and reabsorption takes place between Ce^{3+} and Nd^{3+} in CeF_3 crystal [49]. The luminescence energy of Ce^{3+} ion at some wavelengths is partially absorbed by Nd^{3+} ion, which can absorb energy through the luminescence effect of spontaneous radiation. Therefore, Ce^{3+} ion energy transfer is beneficial to Nd^{3+} ion emission enhancement in near-infrared band. When Ce^{3+} ions absorb energy, the non-radiative transition to the 5d level, Ce^{3+} ions obtain energy transition to the second level 5d level, and then continuously decay back to $^2F_{5/2}$ level. Part of the wavelength will be absorbed by Nd^{3+} ions through radiative energy transfer and transferred to Nd^{3+} ions $^2G_{7/2}$ level. The energy of this level will then jump back to the $^4F_{5/2}$ level, increasing the energy distributed on this level. When excited at 808 nm, the energy of Nd^{3+} ion jumps to $^4F_{5/2}$ level and returns to $^4F_{3/2}$ level through non-radiative relaxation. It then transitions to the ground

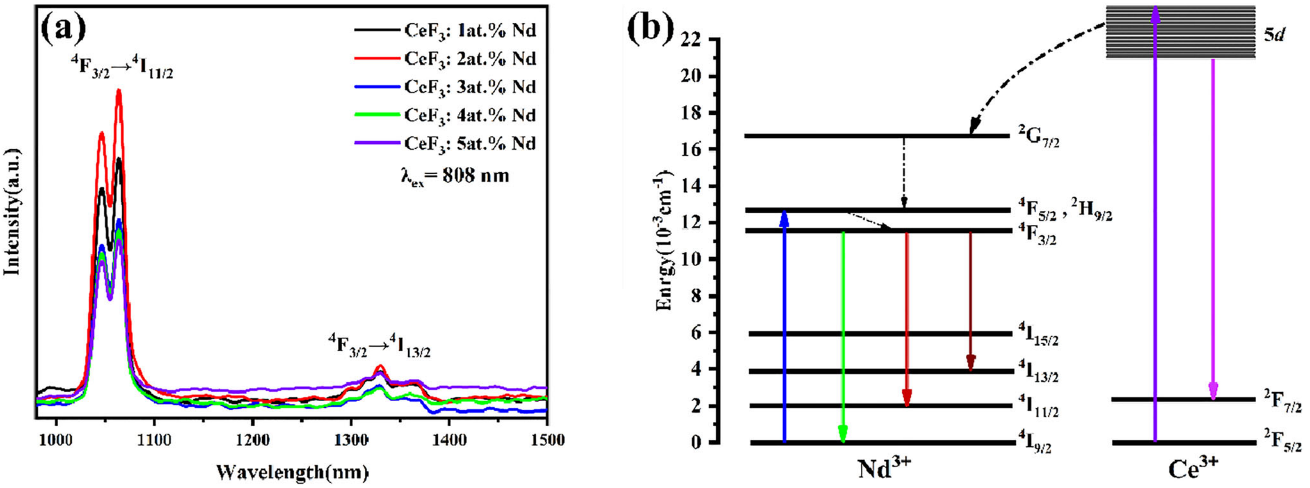

Fig. 12 **a** Near-infrared emission spectra of CeF_3 crystals doped with different Nd^{3+} ion concentrations, the excitation wavelength is 808 nm; **b** The transition energy levels in the crystal and the transition and energy transfer relationship between Ce^{3+} and Nd^{3+} ions

state level and produces near-infrared light: the emission at 900, 1064 and 1330 nm corresponds to the attenuation of the ${}^4F_{3/4}$ energy level to ${}^4I_{9/2}$, ${}^4I_{11/2}$ and ${}^4I_{13/2}$, respectively.

The luminescence performance of Er^{3+}:CeF_3 crystal in near-infrared band is shown in Fig. 13a. The emission wavelength is about 1450–1650 nm, and the emission intensity is strongest at the central wavelength of 1550 nm. The emission in this band originates from the radiative transition from ${}^4I_{13/2}$ to ${}^4I_{15/2}$ levels in the Er^{3+} ion [41]. It can be seen that as the Er^{3+} ion doping concentration increases from 1 to 3at.%, the emission intensity increases continuously, and when it reaches 3at. %, the emission intensity is the strongest. Then, with the increase of Er^{3+} ion doping concentration from 3 to 5 at%, the emission intensity decreases instead of rising, which is because of the reduction of emission intensity caused by concentration quenching. When Ce^{3+} and Er^{3+} ions are in the same matrix, there will be energy transfer in the luminescence process due to the overlap between the energy levels [42]. Therefore, the role of Ce^{3+} ions in NIR luminescence needs to be considered. Figure 13b shows the transition and energy transfer relationship between Ce^{3+} and Er^{3+} ions in the crystal. Under the excitation of 980 nm, Er^{3+} ion absorbs energy to excite a large number of electrons in the ground state of ${}^4I_{15/2}$ to the ${}^4I_{11/2}$ energy level, and a few electrons directly transition to the ${}^4I_{13/2}$ energy level and return to the ground state, emitting a weak 1550 nm infrared light [43]. The energy of Er^{3+} ion at ${}^4I_{11/2}$ energy level is transferred to higher ${}^4F_{7/2}$ energy level through energy transfer, and part of the energy is transferred back to ${}^2H_{11/2}$ and ${}^4S_{3/2}$ energy level as non-radiative transition, and the radiative transition produces green light emission. Other energies continue back to the ${}^4F_{9/2}$ level as a non-radiative transition, which produces a red emission band. Due to the low energy level difference between ${}^3S_{1/2}$ energy level and ${}^4F_{9/2}$ energy level in Er^{3+} ion, the probability of non-radiative transition from ${}^3S_{1/2}$ energy level to ${}^4F_{9/2}$ energy level in Er^{3+} ion is low [44]. In addition, the energy level difference between the ${}^2F_{5/2}$ and ${}^2F_{7/2}$ levels of Ce^{3+} ion and the ${}^4I_{11/2}$ and ${}^4I_{13/2}$ levels of Er^{3+} ion is about 3–4 maximum phonon energies. In general, when the two ions co-exist, there will be an effective cross relaxation between the two energy levels, resulting in an increase in the probability of a non-radiative transition from ${}^4I_{11/2}$ to ${}^4I_{13/2}$ [45]. As a result, the population electron number at ${}^4I_{13/2}$ energy level increases significantly, resulting in stronger 1550 nm NIR emission when the transition back to ${}^4I_{15/2}$ energy level.

3.7 Luminescence decay curve analysis

In order to further study the influence of energy transfer and doping ions on near-infrared luminescence, the luminescence decay curve was tested and analyzed, as shown in Fig. 14. When the test data are fitted by the triple exponential equation, the fitting degree is the best, and the formula (1) is as follows:

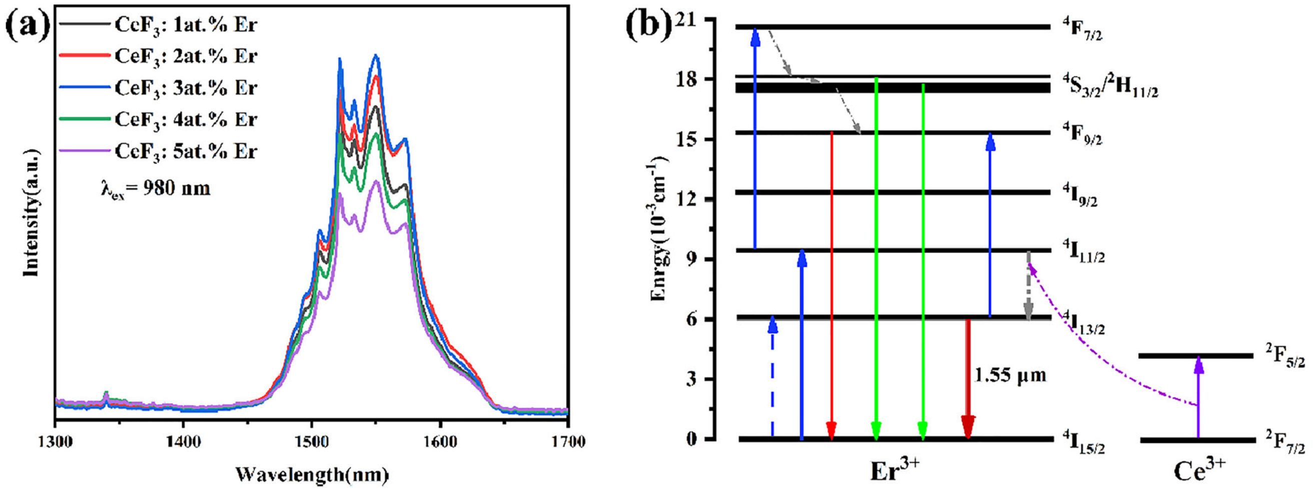

Fig. 13 **a** Near-infrared emission spectra of CeF_3 crystals doped with different Er^{3+} ion concentrations, the excitation wavelength is 980 nm; **b** Transition energy levels in crystals and transition and energy transfer relationships between Ce^{3+} and Er^{3+} ions

$$y = A_1 \times exp\left(\frac{-x}{t_1}\right) + A_2 \times exp\left(\frac{-x}{t_2}\right) + A_3 \times exp\left(\frac{-x}{t_3}\right) + y_0 \tag{1}$$

Get the parameters $A_{1,2,3}$ and $t_{1,2,3}$. According to the calculation formula (2) of three-index luminescence lifetime.

$$\tau = \frac{A_1 {t_1}^2 + A_2 {t_2}^2 + A_3 {t_3}^2}{A_1 t_1 + A_2 t_2 + A_3 t_3} \tag{2}$$

The luminescence attenuation curve and lifetime of Nd^{3+}:CeF_3 crystal are shown in Fig. 14a. The corresponding excitation wavelength is 808 nm, the emission wavelength is 1064 nm, and the corresponding transition energy level is $^4F_{3/2}{\rightarrow}^4I_{11/2}$ It can be seen that with the increase of doping concentration of Nd^{3+} ions, the luminescence lifetime gradually increases, from 4.51×10^{-2} to 8.29×10^{-2} ms, which indicates that with the increase of doping concentration, the distance between Nd^{3+} ions in the crystal lattice decreases, the energy transfer efficiency increases, and the energy on the upper level increases, so it shows a higher attenuation lifetime during emission. In addition, with the increase of Nd^{3+} ion doping concentration, the local Nd^{3+} ion concentration in the crystal increases. Therefore, the relaxation between adjacent Nd^{3+} ions is more likely to occur.

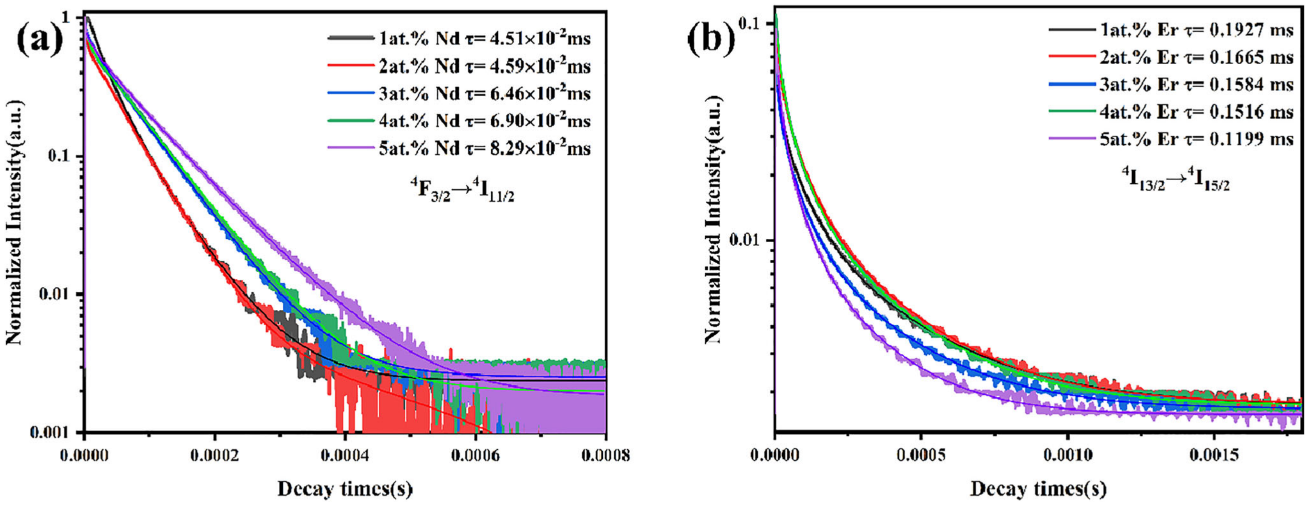

Fig. 14 **a** Fluorescence attenuation curve and lifetime of Nd^{3+}:CeF_3 crystal; **b** Fluorescence attenuation curve and lifetime of Er^{3+}:CeF_3 crystal

This leads to a decrease in the probability of non-radiative transitions, resulting in an increase in decay time and an increase in NIR luminescence. This indicates that it is effective to increase the luminescence lifetime of Nd^{3+} ions by appropriately increasing the doping concentration. Figure 14**b** shows the attenuation curve of Er^{3+}:CeF_3 crystal. The excitation wavelength is 980 nm (corresponding to the energy level $^4I_{13/2}$), and the corresponding transition emission wavelength is 1550 nm (corresponding to the energy level $^4I_{15/2}$). Different from Nd^{3+}:CeF_3 crystal, when the doping concentration of Er^{3+} increases from 1 to 5 at%, as the acceptor of energy transfer, the luminescence decays faster and the lifetime decreases. This is attributed to the fact that with the increase of doping concentration, the effective distance between Er^{3+} ions are shortened, which leads to the reduction of energy transfer time, the increase of the overall efficiency of energy transfer, and the stronger energy transfer effect. Although the luminous intensity becomes stronger, the luminescence lifetime shows a decreasing trend [12]. Another possibility is that with the increase of the doping concentration of Er^{3+} ions, although the radius difference between Ce^{3+} ions and Er^{3+} ions is small, when the doping concentration increases, it will still cause some lattice distortion, which will lead to a large number of dislocations and defects, which is also the reason for the shortened luminescence lifetime.

3.8 Concentration quenching and energy transfer mechanism

Increasing doping concentration will cause the change or even decrease of luminous intensity, which is due to the concentration quenching caused by too high doping concentration. On the one hand, the reverse energy transfer between doped ions and Ce^{3+} ions in the matrix is intensified due to the high doping concentration; on the other hand, the interaction between ions and the non-radiative energy transfer are intensified due to the high doping concentration. Although the interaction is stronger, the overall luminous effect decreases. Figure 15 can vividly express this phenomenon.

According to Dexter's multi-level interaction theory and Reisfeld's approximate correlation theory, generally, the non-radiative energy transfer process in luminescent materials is caused by three effects: exchange interaction, radiation reabsorption and multi-level interaction [22]. To determine the energy transfer mechanism and interaction mechanism of rare earth ions in these two crystals, the critical distance of rare earth ions is first calculated, and the formula (3) is.

$$R_c \approx 2\left[\frac{3V}{4\pi X_c Z}\right]^{\frac{1}{3}} \tag{3}$$

In the formula, V represents the unit cell volume of CeF_3 nanoparticles, and X_c is the total concentration (critical concentration) of doped ions. Z is the number of cations in the center of the unit cell. According to the standard card (JCPDS 08-0045), the V and Z values of CeF_3 are 318.9 and 6, respectively. For the critical distance (R_c) of Nd^{3+} and Er^{3+} ions in the CeF_3 crystal. According to the calculation, the results are 12.6610 and 15.0153 Å. This shows that when the two rare earth ions are doped, the critical distance between the ions is greater than 5 Å, and there is no forbidden band transition at this time. The concentration quenching effect mainly comes from the electrical interaction between rare earth ions in the crystal [5]. According to Dexter's theory, when the electric interaction is identified as the main cause of the concentration quenching effect, it can be refined into three kinds of interactions. These three different interactions can be calculated and distinguished according to Eq. (4).

$$\frac{I}{X} = K[1 + \beta(x)^{\frac{\theta}{3}}]^{-1} \tag{4}$$

Equation (4) can be simplified and transformed into Eq. (5) as follows:

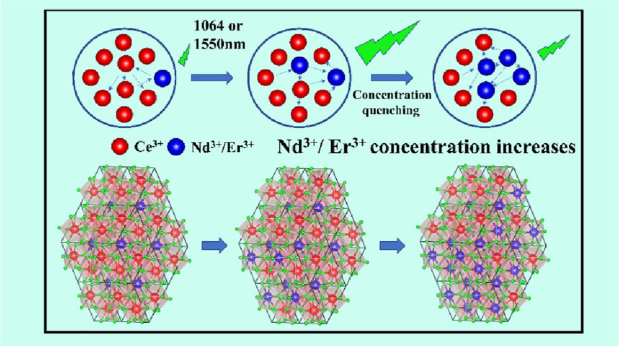

Fig. 15 schematic diagram of concentration quenching of rare earth ion-doped CeF_3 crystal

$$\log\left(\frac{I}{x}\right) = A - \frac{\theta}{3}\log x, \qquad (5)$$

where I is the emission intensity, x is the sensitizer concentration, and K and β are the matrix constants under the same excitation conditions. When θ is close to 6, 8 and 10, the interaction types correspond to dipole-dipole interaction, dipole-quadrupole interaction and quadrupole-quadrupole interaction, respectively. The corresponding data are calculated by Eq. (5) and linearly fitted, as shown in Fig. 16. It is shown in Fig. 16a that the θ/3 slope of Nd:CeF_3 crystal is 1.3965 ± 0.16, and the θ value is equal to 4.1085 ± 0.48. In the Fig. 16b, the slope θ/3 of Er^{3+}: CeF_3 crystal is -1 ± 1.27 × 10^{-15} and the θ value is about − 3 by fitting the data. This indicates that the electric interaction of the doped rare earth ions Nd^{3+} or Er^{3+} in the CeF_3 crystal belongs to dipole-dipole interaction.

3.9 J-O parameter calculation

Judd-ofelt theory has been widely used to predict and evaluate the effects of rare earth ions on the crystal field environment and luminescence properties [46–48]. It is important to estimate useful luminescence information from the calculated parameters Ω_t (t = 2, 4, 6). Generally, these parameters can be estimated based on the absorption spectra of rare earth ions and the theoretical values of the intrinsic tensor operators $U^{(2)}$, $U^{(4)}$ and $U^{(6)}$ of rare earth ions. The experimental vibrator strengths S_{exp} and theoretical vibrator strengths f_{cal} from the ground state transition (LJ) to the excited state (L′J′) can be calculated by Eqs. (6) and (7).

$$S_{exp}(J \rightarrow J') = \frac{3hc(2J+1)}{8\pi^3 e^2}\frac{9n}{(n^2+2)^2\bar{\lambda}}\frac{1}{0.43N_0 l}\int OD(\lambda)d\lambda \qquad (6)$$

$$f_{cal} = f_{ed} + f_{md} = \frac{8\pi^2 mcv}{3he^2(2J+1)}\left(\frac{(n^2+2)^2}{9n}S_{ed} + nS_{md}\right) \qquad (7)$$

In the formula, e and m represent the charge and mass of the electron, c represents the speed of light, h is Planck's constant, J is the total angular momentum of the ground state, and n represents the refractive index. $(n^2+2)^2/9n$ and n are used to correct the local fields of electric and magnetic dipole absorption transitions. f_{ed} and f_{md} represent the intensity of electric and magnetic dipole transitions, S_{ed} and S_{md} represent the intensity of electric and magnetic dipole transitions, respectively. Since the intensity of magnetic dipole transition is very low compared with that of electric dipole transition, it can be ignored and does not affect the variation trend of the calculated value. It is calculated by Eq. (8).

$$f_{ed}(J \rightarrow J') = \sum_{t=2,4,6}\Omega_t\left|\left\langle 4f^n[S,L]JU^{(t)}4f^n[S',L']J'\right\rangle\right|^2 \qquad (8)$$

$||U_t||^2$ is a tensor operator, is obtained by approximate coupling calculation (rare earth ions

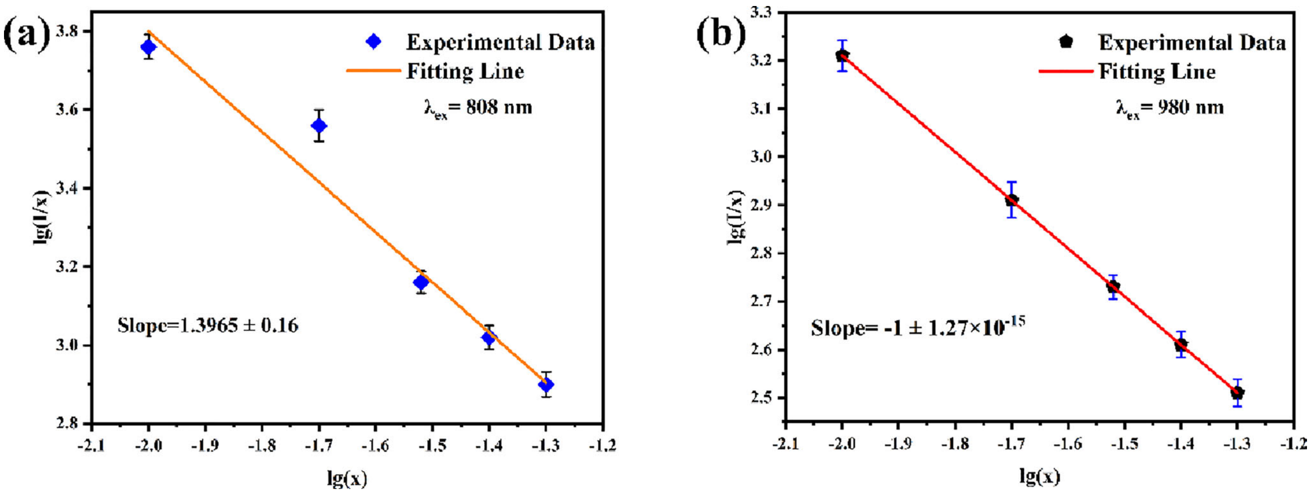

Fig. 16 **a** Nd^{3+}:CeF_3 crystal, logarithmic ratio of emission intensity to doping concentration and its fitting curve; **b** Er^{3+}:CeF_3 crystal, logarithmic ratio of emission intensity to doping concentration and its fitting curve

from (LJ) to (L 'J') state transition process). The values of tensor operators are derived from the inherent properties of rare earth ions and are determined by the electronic structure of rare earth ions themselves, which is not affected by the matrix structure. The approximate values in different matrices do not affect the calculation results during matrix calculation. The J-O strength parameters of Nd^{3+} or Er^{3+} doped CeF_3 crystals with different concentrations can be obtained by solving the equations. The calculation results of Ω_t (t = 2, 4, 6) values are listed in Tables 2 and 3.

Ω_t can reflect some properties of coordination field, electron wave function and energy level splitting in crystal materials, and could calculate some important optical parameters. Ω_2 is usually closely related to the symmetry and order of the coordination field. The stronger the covalent bond, the weaker the covalent bond between rare earth atom and matrix, and the smaller the calculated Ω_2. Therefore, according to the calculated values of Ω_2, Nd^{3+}:CeF_3 and Er^{3+}:CeF_3 crystals are typical ionic crystals with very weak covalent bonds. In addition, the values of Ω_4 and Ω_6 decrease gradually with the increase in doping concentration. This indicates that the crystal basicity increases with the increase in doping concentration, and the ability of doping to lead to the gain and loss of electrons in the crystal is stronger. When electrons are more active, they take part in the completion of radiative and non-radiative transitions more intensely. This also confirms that when the doping concentration increases, the electron active state in the internal structure intensifies and the luminescence intensity changes significantly.

Table 2 Ω_t (t = 2, 4, 6) values of Nd^{3+}:CeF_3 crystal

Crystal	Ω_2	Ω_4	Ω_6	Error δ ($\times 10^{-6}$)
1at. %Nd^{3+}:CeF_3	0.15	0.99	0.27	0.42
2at. %Nd^{3+}:CeF_3	0.08	0.68	0.64	0.28
3at. %Nd^{3+}:CeF_3	0.19	0.48	0.72	0.34
4at. %Nd^{3+}:CeF_3	0.10	0.28	0.31	0.19
5at. %Nd^{3+}:CeF_3	0.15	0.42	0.61	0.30

Table 3 Ω_t (t = 2, 4, 6) values of Er^{3+}:CeF_3 crystal

Crystal	Ω_2	Ω_4	Ω_6	Error δ ($\times 10^{-6}$)
1at. %Er^{3+}:CeF_3	0.1	0.86	0.8	1.01
2at. %Er^{3+}:CeF_3	0.16	0.52	0.77	0.71
3at. %Er^{3+}:CeF_3	0.32	0.77	1.01	0.67
4at. %Er^{3+}:CeF_3	0.02	0.38	0.65	0.62
5at. %Er^{3+}:CeF_3	0.03	0.42	0.51	0.46

4 Conclusion

A series of CeF_3 crystals doped with Nd^{3+} or Er^{3+} ions were grown by the Bridgman method. The XRD, Raman and density parameters of the crystal were measured. The results showed that the doping of the two ions did not change the hexagonal phase structure, but only replaced the Ce^{3+} ion in the matrix. It is found that the maximum phonon frequency of Nd^{3+}:CeF_3 crystal is only 388 cm^{-1}, and the maximum phonon frequency of Er^{3+}:CeF_3 crystal is only 392 cm^{-1}, which is far less than that of ordinary oxide crystals. The charge densities, band gap values (2.91 and 4.37 eV) and total state densities of the two crystals were obtained by first-principles simulations. The difference between the calculated band gap width and the measured results is small, which can well explain the energy level change caused by rare earth ion doping and its influence on the near-infrared luminescence performance. The results of absorption and emission spectra show that Nd^{3+}:CeF_3 crystal exhibits high near-infrared emission at 1064 nm, and the best luminescence intensity is achieved when the doping concentration is 2 at%. Er^{3+}:CeF_3 crystals exhibit a near-infrared wideband emission of 1550 nm, and the luminescence intensity reaches its maximum when the concentration is about 3 at%. When the doping concentration of the two crystals is further increased, the luminescence intensity decreases and the concentration quenching occurs. According to energy transfer theory and concentration quenching mechanism, both crystals belong to the dipole-dipole electrical interaction. The J-O strength parameters are calculated and the influence of doping concentration on structure and stability is revealed. In summary, the test and calculation verification show that Nd^{3+}:CeF_3 and Er^{3+}:CeF_3 has stable crystal properties and excellent luminous effects in the near-infrared band. It is a kind of excellent laser crystal material and has great application value in the laser field.

Acknowledgements

This work was supported by Government Funded Projects (627010104), International Science and Technology Cooperation Project of Jilin Province Science, Technology Department (20200801038GH), The Open Project of State Key Laboratory of Inorganic Synthesis and Preparative Chemistry (Jilin University) (No.2021-19). Thanks to Professor Ligong Zhang, Changchun Institute of Optics, Fine Mechanics and Physics, Chinese Academy of Sciences for his help in testing.

Author contribution

WY Conceptualization, Data curation, Formal analysis, Writing - original draft, Later revision, English translation, theoretical calculation. Crystal growth experiment. XJ Supplementary experimental data, data test. Literature search, data collection. Crystal growth experiment. ZL Investigation, Supplementary experimental data, data test. Crystal growth experiment. HL Supplementary experimental data, data test. CL Investigation, Methodology. Literature search, data collection. ZS Structural model optimization, first-principles simulation, Data processing, Theoretical analysis. KH Project funding, theoretical guidance. FZ Conceptualization, Supervision, Funding acquisition, Resources, Supervision, Manuscript revision, theoretical guidance. CL Conceptualization, Supervision, Funding acquisition, Resources, Supervision, test guide HL Investigation, Methodology. ZS Conceptualization, Supervision, Funding acquisition, Resources, Supervision.

Funding

The authors have not disclosed any funding.

Data availability

The data that support the findings of this study are available from the corresponding author upon reasonable request. All data generated or analysed during this study are included in this published article [and its supplementary information files].

Declarations

Conflict of interest The manuscript has not been published previously by any of the authors and/or is not under consideration for publication in another journal at the time of this submission. No conflict of interest exits in the submission of this manuscript, and manuscript is approved by all authors for publication.

Ethical approval I, the Corresponding Author, declare that this manuscript is original, has not been published before and is not currently being considered for publication elsewhere. I can confirm that the manuscript has been read and approved by all named authors and that there are no other persons who satisfied the criteria for authorship but are not listed. I further confirm that the order of authors listed in the manuscript has been approved by all of us. I understand that the Corresponding Author is the sole contact for the Editorial process and is responsible for communicating with the other authors about progress, submissions of revisions and final approval of proofs. Signed by the Corresponding Author on behalf of the all other authors.

References

1. A.A. Ansari, Influence of surface functionalization on structural and photo-luminescence properties of CeF_3: Tb nanoparticles. Appl. Surf. Sci. **409**, 285–290 (2017)
2. W. Li, M. Chen, H.M. Kou, J. Liu, Y. Shi, X.Q. Feng, Y.B. Pan, J.K. Guo, Translucent ccerium fluoride ceramics fabricated by hot-pressing for scintillation application. Int. J. Appl. Ceram. Tec. **12**(3), 638–642 (2015)
3. G. Zhao, C.C. Zhao, Y.L. Yang, M. Xu, S.M. Li, Y. Hang, Magneto-optical performances of novel neodymium-doped CeF_3 crystal. Mater Lett **300**, 130134 (2021)
4. X.J. Li, W.Q. Zhang, L.M. Dong, D.Y. Liu, Z.G. Qi, Low temperature molten salt synthesis of CeF_3 and CeF_3: Tb^{3+} phosphors with efficient luminescence properties. J. Lumin **205**, 122–128 (2019)
5. Z. Leng, X.Y. Wang, W.L. Yang, W.J. Yang, T.Q. Zhang, X.L. Jiang, F.M. Zeng, C. Li, H. Lin, Z.M. Su, Study on the optical properties of Er, Yb: $KY(WO_4)_2$ nanoparticles doped with different concentrations of Na^+ ions. J Lumin **238**, 118160 (2021)

6. S. Rahelehyousefi, H.A. Abbasalshamsi, Green sonochemical synthesis of $BaDy_2$ NiO_5/Dy_2O_3 and $BaDy_2NiO_5/NiO$ nanocomposites in the presence of core almond as a capping agent and their application as photocatalysts for the removal of organic dyes in water. RSC Adv **11**, 11500 (2021)
7. S. Niasari, Sobhani Masoud, A new nanocomposite superionic system ($CdHgI_4/HgI_2$): synthesis, characterization and experimental investigation. Adv. Powder Technol. **28**, 1258 (2017)
8. A. Sry, B. Ma, A. Msm, Hydrothermal synthesis of $DyMn_2O_5/Ba_3Mn_2O_8$ nanocomposite as a potential hydrogen storage material. Int. J. Hydrogen Energ. **44**(43), 24005–24016 (2019)
9. A. Sry, B. Haa, C. Oa et al., Synthesis, characterization and application of Co/Co_3O_4 nanocomposites as an effective photocatalyst for discoloration of organic dye contaminants in wastewater and antibacterial properties. J Mol Liq **337**, 116405 (2021)
10. S.R. Yousefi, O. Amiri, M.S. Niasari, Control sonochemical parameter to prepare pure $Zn_{0.35}Fe_{2.65}O_4$ nanostructures and study their photocatalytic activity. Ultrason. Sonochem **58**, 104619 (2019)
11. S.R. Yousefi, M. Ghanbari, O. Amiri, Z. Marzhoseyni, P. Mehdizadeh, M.H. Oghaz, M.S. Niasari, $Dy_2BaCuO_5/Ba_4DyCu_3O_{9.09}$ S-scheme heterojunction nanocomposite with enhanced photocatalytic and antibacterial activities. Am. Ceram. Soc. **104**, 2952–2965 (2021)
12. S.R. Yousefi, D. Ghanbari, Photo-degradation of organic dyes: simple chemical synthesis of $Ni(OH)_2$ nanoparticles, $Ni/Ni(OH)_2$ and Ni/NiO magnetic nanocomposites. J. Mater. Sci. Mater. El **27**(2), 1–10 (2015)
13. A. Mam, B. Sry, A. Lsj, Green synthesis of $DyBa_2Fe_3O_{7.988}/DyFeO_3$ nanocomposites using almond extract with dual eco-friendly applications: photocatalytic and antibacterial activities. Int. J. Hydrogen Energy **47**, 14319 (2022)
14. S.R. Yousefi, D. Ghanbari, M.S. Niasari, Hydrothermal synthesis of nickel hydroxide nanostructures and flame retardant poly vinyl alcohol and cellulose acetate nanocomposites. J. Nano. **6**(1), 77 (2016)
15. E.G. Villora, K. Shimamura, G.R. Plaza, Ultraviolet-visible optical isolators based on CeF_3 Faraday rotator. J. Appl. Phys. **117**(23), 233101 (2015)
16. E.A. Mironov, A.V. Starobor, I.L. Snetkov, O.V. Palashov, H. Furuse, S. Tokita, R. Yasuhara, Thermo-optical and magneto-optical characteristics of CeF_3 crystal. Opt. Mater. **69**, 196–201 (2017)
17. C. Bartha, C. Secu, E. Matei, C. Negrila, A. Leca, M. Secu, Towards a correlation between structural, magnetic, and luminescence properties of CeF_3:Tb^{3+} ^{n}anocrystals. Materials **13**(13), 2980 (2020)
18. C.Y. Zhang, Q. Jiang, X.Y. Wang, J. Liu, Y.T. Xiao, C. Li, H. Lin, F.M. Zeng, Z.M. Su, A novel scheme to acquire enhanced up-conversion emissions of Ho^{3+} and Yb^{3+} co-doped Sc. Curr. Appl. Phys. **$_2O_3$**(20), 82–88 (2020)
19. D.N. Karimov, D.S. Lisovenko, A.G. Ivanova, V.V. Grebenev, P.A. Popov, N.L. Sizova, Bridgman growth and physical properties anisotropy of CeF_3single crystals. Crystals **11**(7), 793 (2021)
20. M.H. Zhong, Z.D. Wang, D. Dai, B.Z. Yang, S.X. Zuo, C. Yao, F.Q. Wu, X.Z. Li, Up-conversion hollow nanospheres CeF_3 co-doped with Yb^{3+} and Tm^{3+} for photocatalytic nitrogen fixation. J. Rare Earth **40**, 586–594 (2022)
21. X.L. Jiang, X.Y. Wang, X.M. Shi, H.Y. Sha, W.J. Yang, W.L. Yang, Z. Leng, H. Lin, Z.M. Su, C. Li, F.M. Zeng, Effect of Mn^{4+} ions on the structure and luminescence properties of $NaY(MoO_4)_2$: Yb^{3+}/Er^{3+} phosphor. Opt. Mater **113**, 110873 (2021)
22. C. Pedrini, A.N. Belsky, B. Moine, D. Bouttet, Fluorescence processes and scintillation of CeF_3crystal excited by UV and X-ray synchrotron radiation. Acta. Phys. Pol. A. **84**(5), 953–958 (1993)
23. Y. Chen, T.M. Liu, C.L. Chen, R. Sun, S.H. Lv, M. Saito, S. Tsukimoto, Z.C. Wang, Facile synthesis of hybrid hexagonal CeF_3 nano-disks on CeO_2 frustum pyramids. Mater. Lett. **92**, 7–10 (2013)
24. C.Y. Zhang, X.Y. Wang, C. Li, H. Lin, F.M. Zeng, Z.M. Su, Effect of Li ions on structure and spectroscopic properties of $NaY(WO_4)_2$: Yb/Ho phosphor. Ceram. Int. **46**(15), 24248–24256 (2020)
25. W.L. Yang, Z.Y. Zhang, X. Zhang, X.T. Wang, X.L. Jiang, Z. Leng, H. Lin, F.M. Zeng, C. Li, Z.M. Su, Enhancement of fluorescence and magnetic properties of CeF_3: RE^{3+} (Tb, Gd) nanoparticles via multi-band UV excitation and Li doping regulation. Ceram. Int. **47**, 16450–16459 (2021)
26. P. Molina, V. Vasyliev, E.G. Víllora, K. Shimamura, CeF_3 and PrF_3 as UV-visible Faraday rotators. Opt Express **19**(12), 11786–11791 (2011)
27. Y.L. Yang, L.H. Zhang, S.M. Li, S.L. Zhang, P.X. Zhang, M.Z. He, M. Xu, Y. Hang, Crystal growth and 570 nm emission of Dy^{3+} doped CeF_3 single crystal. J. Lumin. **215**, 116707 (2019)
28. H.F. Li, J.Y. Wang, J.F. Chen, Y. Dai, L.B. Su, X. Li, A.M. Kalashnikova, A.H. Wu, Bridgman growth and magneto-optical properties of CeF_3 crystal as Faraday Rotator. Opt Mater **100**, 109675 (2020)
29. K. Nakada, Y. Matsumoto, Y. Shimoi, K. Yamada, Y. Furukawa, Temperature-dependent evolution of Raman spectra of methylammonium lead halide perovskites, $CH_3NH_3PbX_3$($X = I$, Br). Molecules **24**(3), 626 (2019)

30. H. Zhang, S. Duan, P.M. Radjenovic, Q.T. Zhong, J.F. Li, Core–shell nanostructure-enhanced Raman spectroscopy for surface catalysis. Accounts Chem. Res. **53**(4), 729–739 (2020)
31. H.Y. Yang, S.R. Zhang, Y.W. Chen, H.C. Yang, Y. Yuan, E.Z. Li, Crystal chemistry, Raman spectra, and bond characteristics of trirutile-type $Co_{0.5}Ti_{0.5}TaO_4$ microwave dielectric ceramics. Inorg. Chem. **58**(1), 968–976 (2018)
32. P.L. Praveen, D.P. Ojha, Role of molecular interactions and end chain length on the photosensitivity of liquid crystalline alkyl cyanobiphenyl dimers-UV absorption-based approach through DFT calculations. Phase Transit. **87**, 641 (2014)
33. P.L. Praveen, D.P. Ojha, Calculation of spectral shifts in UV-visible region and photoresponsive behaviour of fluorinated liquid crystals: effect of solvent and substituent. Mater Chem. Phys. **135**(2–3), 628–634 (2012)
34. P.L. Praveen, D.P. Ojha, Calculation of spectral shifts in UV-visible region and photo stability of thermotropic liquid crystals: solvent and alkyl chain length effects. J. Mol. Liq. **2012**, 169 (2012)
35. J.T. Jaison, A. Simi, R.M. David, L.P. Praveen, Theoretical model of a nematogen: estimation of phase stability, absorption, electrochemical, and nonlinear optical properties. Acta Phys Pol A **134**(2), 1–7 (2018)
36. P.L. Praveen, 7-Hexyloxy-3-[4’-(3-methylbutyloxy) phenyl]-4H-1-benzopyran-4-one: study of smectic behaviour and UV absorption profile. Mol. Cryst. Liq. Cryst. **667**(1), 44–53 (2018)
37. P.L. Praveen, D.P. Ojha, Optical absorption behavior and spectral shifts of fluorinated liquid crystals in ultraviolet region: A comparative study based on DFT and semiempirical approaches. J. Mol. Liq **194**, 8–12 (2014)
38. P.L. Praveen, D.P. Ojha, Effect of substituent on UV-visible absorption and photostability of liquid crystals: DFT study. Phase Transit. **87**(5), 515 (2014)
39. D. Punyatoya, P.L. Praveen, Theoretical investigation on absorption spectral profile of tetrazole liquid crystals: Hexyl, nonyl end groups and solvent effects. IOP Conference Series Materials Science and Engineering **798**(1), 012041 (2021)
40. P.L. Praveen, Nematic and smectic bithiophenes for UV sensing mechanism: Comparative calculations on different homologues. J. Mol. Liq. **341**, 117424 (2021)
41. H. Miao, G.F. Huang, L. Xu, Y.C. Yang, K. Yang, W.Q. Huang. A novel photocatalyst CeF_3: facile fabrication and photocatalytic performance. RSC Adv. **5**(115), 95171–95177 (2015)
42. C. Li, B. Wang, R. Wang, H. Wang, First-principles studies on the electronic and optical properties of $CeCl_3$ and $CeBr_3$. Solid State Commun. **144**(5–6), 220–224 (2007)
43. S.M. Saini, T. Nautiyal, S. Auluck, Electronic and optical properties of rare earth trifluorides RF_3 (R = La, Ce, Pr, Nd, Gd and Dy). Mater. Chem. Phys. **129**(1–2), 349–355 (2011)
44. Y. Xu, L. Zhou, X. Zhang, B.P. Li, F.F. Huang, S.Q. Xu, Sensitization mechanism of Bi/Nd co-doped germanosilicate glass for infrared applications. Opt. Laser Technol. **130**, 106346 (2020)
45. H.K. Dan, J.B. Qiu, D.C. Zhou, R.F. Wang, Broadband near-infrared emission and energy transfer in Nd-Bi co-doped transparent silicate glass-ceramics for optical amplifiers. Opt Mater. **85**, 517–522 (2018)
46. R. Birang, J. Poursamimi, N. Gutknecht, F. Lampert, M. Mir, Comparative evaluation of the effects of Nd: YAG and Er: YAG laser in dentin hypersensitivity treatment. Lasers Med. Sci. **22**, 21–24 (2007)
47. K. Matthias, G. Hermann, D. Heinz, B. d’Hoedt, Effect of Nd: YAG, Ho: YAG, Er: YAG, CO_2, and GaAlAs laser irradiation on surface properties of endosseous dental implants. Int. J. Oral Max. Impl. **17**, 202–211 (2002)
48. Y.L. Yang, L.H. Zhang, S.M. Li, S.L. Zhang, Y.H. Zhang, Q.N. Fang, M.Z. He, M. Xu, Y. Hang, Growth and mid-infrared luminescence property of Ho^{3+} doped CeF_3 single crystal. Infrared Phys. Technol. **105**, 103230 (2020)
49. X.L. Jiang, Z.Y. Zhang, T.Q. Zhang, C. Li, Z. Leng, W.L. Yang, X.Y. Wang, X.M. Shi, X. Zhang, H.Y. Sha, Z.D. Zhou, H. Lin, K.K. Huang, C. Li, Z.M. Su, F.M. Zeng, Enhanced up-conversion luminescence intensity of $NaY(MoO_4)_2$: Ho^{3+}/Yb^{3+} phosphor by doping with Mg^{2+} ions for use in high-efficiency optical temperature sensor. J. Lumin. **245**, 118759 (2022)